

Article

Beam Position Monitor Characterization for the High Energy Photon Source Synchrotron

Jun He ^{1,*}, Yanfeng Sui ^{1,2,*}, Yong Li ^{1,2}, Huizhou Ma ¹, Yaoyao Du ¹, Xujian Wang ¹, Junhui Yue ¹
and Jianshe Cao ^{1,2}

¹ Institute of High Energy Physics, Chinese Academy of Sciences, Beijing 100049, China

² University of Chinese Academy of Sciences, Beijing 100049, China

* Correspondence: hejun@ihep.ac.cn (J.H.); syf@ihep.ac.cn (Y.S.)

Abstract: Beam position monitor (BPM) characterization has been widely studied at the synchrotron. The characteristic impedance of a stripline BPM was designed using a simulation and measured using the time-domain reflectometer method. The mechanical and electrical parameters of the feedthroughs with the buttons used for the BPMs were measured. Special care was taken in the analysis of the consistency of the four channels of the BPM. The feedthroughs were sorted based on their capacitance values. This paper presents the characterization results of the feedthroughs and BPMs. The electro-mechanical offsets were measured using the Lambertson method, and the calibration coefficients were measured using a stretched wire. The BPM differences introduced during mass production were determined by a statistical analysis of the measurement results.

Keywords: beam position monitor; button; stripline; electro-mechanical offsets



Citation: He, J.; Sui, Y.; Li, Y.; Ma, H.; Du, Y.; Wang, X.; Yue, J.; Cao, J. Beam Position Monitor Characterization for the High Energy Photon Source Synchrotron. *Symmetry* **2023**, *15*, 660. <https://doi.org/10.3390/sym15030660>

Academic Editor: M. D. Rodriguez Frias

Received: 2 February 2023

Revised: 28 February 2023

Accepted: 3 March 2023

Published: 6 March 2023



Copyright: © 2023 by the authors. Licensee MDPI, Basel, Switzerland. This article is an open access article distributed under the terms and conditions of the Creative Commons Attribution (CC BY) license (<https://creativecommons.org/licenses/by/4.0/>).

1. Introduction

A high-performance fourth-generation high energy photon source (HEPS) with an energy of 6 GeV and emittance of 34 pm-rad is under construction in Huairou, Beijing, by Institute of High Energy Physics [1,2]. More than 700 beam position monitors (BPMs) will be used for the beam orbit measurements [3,4], fast orbit feedback (FOFB) system [5], bunch current measurements, tuning measurements, bunch feedback and beam loss system.

Table 1 summarizes the distribution of these BPMs for the HEPS. There will be more than 700 BPMs and nearly 3000 feedthroughs. Although manufacturers will provide inspection sheets for their products, the Beam Instrumentation group still tested nearly 1000 feedthroughs and 100 BPMs. Various parameters were measured, including the magnetic permeability, capacitance, mechanical size, characteristic impedance, electrical offset, and sensitivity coefficient. All the feedthroughs and BPMs were engraved with unique serial numbers, and the results were used to track the quality of the BPMs.

The BPM system has many error sources, including pickup fabrication error, connector contact error, cable impedance error, pickup setting error, and signal processor error. In this paper, we introduce various characterizations of the HEPS BPMs and our effort to control the fabrication error. Table 2 shows the specification of the BPMs of the HEPS. The most important requirements are the resolution during normal operation and accuracy during the preliminary commissioning phase. The beam size in the vertical direction is approximately 1 μm , the stability of the optical axis requirement is 1/10 of the beam size, which is 0.1 μm [6].

The field gradients of the quadrupole and sextupole in an MBA lattice are significantly larger than those of the third-generation light source. The tolerances for the misalignment of the quadrupole and sextupole are significantly more stringent. The tolerances for BPMs are at the same level in the commissioning stage [7]. The tolerances of the quadrupole and sextupole are $\pm 30 \mu\text{m}$ [8,9]. The error budget of the BPMs is 200 μm (RMS) [10,11].

The resolution (standard deviations) requirement for a slow closed orbit position (5 Hz bandwidth, 10 Hz data update rate) is less than 0.1 μm . For a fast closed orbit position (5 kHz bandwidth, 22 kHz data update rate), the resolution requirement is less than 0.3 μm . For a turn-by-turn position (66 kHz bandwidth, 220 kHz data update rate) it is less than 1 μm [3]. The HEPS has two different operation modes: high brightness and high bunch charge. The bunch charges for these two modes are 1.33 and 14 nC, respectively [12]. The dynamic range requirement is 50 dB. In addition, the requirements for the permeability (μ_r) and hermeticity are <1.02 and $<1 \times 10^{-11} \text{ Pa}\cdot\text{m}^3 \text{ s}^{-1}$, respectively.

Table 1. Number and type of the BPMs.

Instruments		LINAC	LTB	BTS	STB	Dump Line	Booster	Storage Ring
BPM	Button	2	0	0	0	0	79	588
	Stripline	6	8	11	11	2	1	0

Table 2. Specification of the HEPS BPMs.

	Parameter	Requirement	Instruction
Strip	Resolution	$<30 \mu\text{m}$	$>500 \text{ pC}$
	Accuracy	$<200 \mu\text{m}$	$>500 \text{ pC}$
	Linear range	$\pm 6 \text{ mm}$	Reading error $< 200 \mu\text{m}$ with a linear fitting
	Dynamic range	50 dB	Single bunch 0.05–18 nC
Button BPM for storage ring	Resolution	$<0.1 \mu\text{m}$ $<0.3 \mu\text{m}$ $<1 \mu\text{m}$	Update rate 10 Hz, 200 mA Update rate 22 kHz, 200 mA Update rate 220 kHz, 200 mA
	First turn	$<500 \mu\text{m}$	0.05 nC Bunch charge
	BPM alignment accuracy [8,9]	$<30 \mu\text{m} (x/y)$	Related to the adjacent quadrupole
		$<150 \mu\text{m} (z)$	Related to the adjacent quadrupole
		0.2 mrad	Pitch/yaw/roll
	Hermeticity	$<1 \times 10^{-11} \text{ Pa}\cdot\text{m}^3 \text{ s}^{-1}$	He
	Dynamic range	50 dB	0.05–15 nC
	Linear range	$\pm 3 \text{ mm}$	Reading error $< 200 \mu\text{m}$ with a linear fitting
Permittivity μ_r	<1.02 *	<1.05 at few special points such as the welding spot	

* Overall requirements of vacuum pipes for storage ring.

2. Linac and Transport Line BPM Characterization

There are 38 BPMs in the linac and three transport lines. To ensure that the impedance of a stripline electrode was 50 Ω , electromagnetic simulation software from Computer Simulation Technology (CST) was used to the impedance calculation of the striplines [13]. The mechanical parameters designed based on the CST calculations are listed in Table 3. Figure 1a,b present a schematic showing the symbols listed in Table 3 and mechanical diagram of the stripline BPM, respectively. Figure 1c shows the characteristic impedance results for the stripline obtained using the time-domain reflectometer (TDR) method and calculated using a CST simulation. Three BPMs, including 12 stripline electrodes, are listed, and the CST simulation results are translated along the vertical axis with an amplitude of 10 Ω to distinguish them from the measured values. To determine the boundary between the feedthroughs and cable, the results for the open-circuit cable are listed, and the result for the stripline electrode was obtained by connecting the feedthroughs to the coaxial

cable. The bandwidth and the rise time (τ_{rise}) of the CST simulation was 35 GHz and 25 ps, respectively. The spatial resolutions for vacuum (air) and ceramic with ϵ_r values of 1 and 9 were 7.5 and 2.5 mm, respectively. The TDR test was conducted using a Tektronix DSA8200 digital serial analyzer with a nominal rise time of 35 ps.

Table 3. Mechanical size of the striplines.

Location	r_{in} [mm]	t [mm]	h [mm]	L_{strip} [mm]	α [°]	θ^* [°]	$Z^{**\text{strip}}$ [Ω]
Linac and transport line between the linac and the booster	15	1.5	2.2	150	30	0	50.8
Transport line between the booster and the ring	13	1.5	1.9	100	30	0	49.9
Dump line	25	1.5	3.3	150	30	45	49.9

* The angle between adjacent electrodes was 90°. ** CST results.

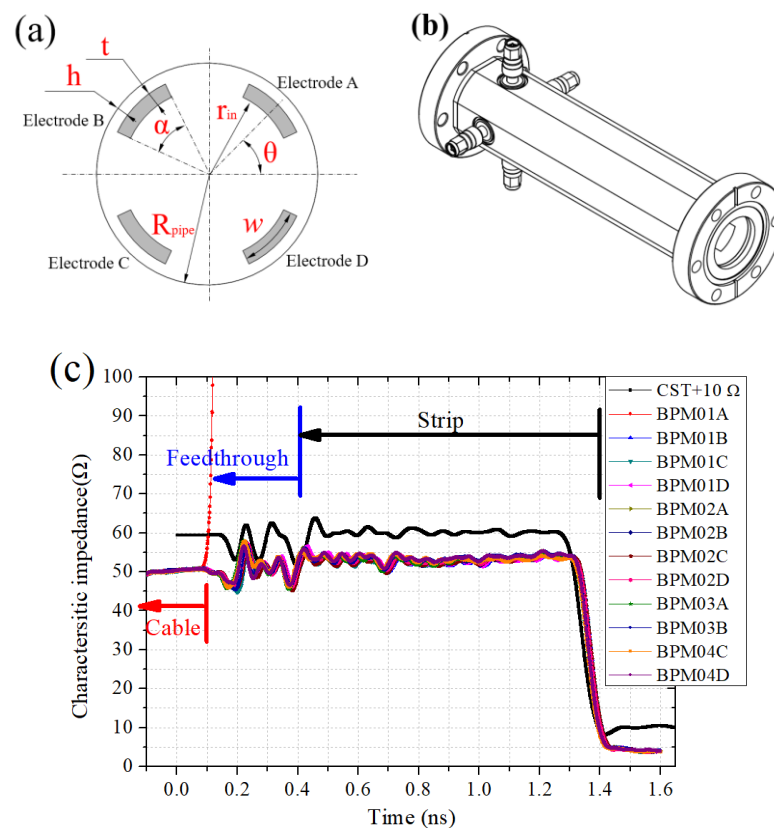


Figure 1. (a) Schematic of stripline BPM. (b) Mechanical design drawing. (c) TDR measurement results for three stripline BPMs and CST simulation results.

In a TDR measurement, when a transverse electromagnetic wave travels through a device under test, the time represents the electrical length. In Figure 1c, the time ranges of 0–0.1, 0.1–0.4 and 0.4–1.4 ns correspond to the cable, feedthrough, and stripline electrode, respectively. The characteristic impedance of the stripline was slightly larger than 50 Ω (50–55 Ω). We measured the impedance of all the striplines. The nominal time resolution of the TDR measurement was 0.5 ps, and there were 1600 points between 0.5 and 1.3 ns, which corresponded to the stripline electrode. The average and standard deviation (STD) of a single-stripline electrode are shown in Figure 2a. All the impedances of the 152 electrodes were in the range of 51–54 Ω , and the standard deviation was 0.7–1 Ω . According to the CST calculation results, when all the other parameters were kept constant (the standard

value listed in Table 3), an impedance deviation of $\pm 1 \Omega$ corresponded to a mechanical size deviation of $\pm 80 \mu\text{m}$ for h or $\pm 70 \mu\text{m}$ for t . If we assume that the impedance deviation was caused by the error in cover angle α , the deviation was approximately $\pm 1^\circ$. The positioning and machining accuracies of the stripline electrode could be inferred from the above analysis results.

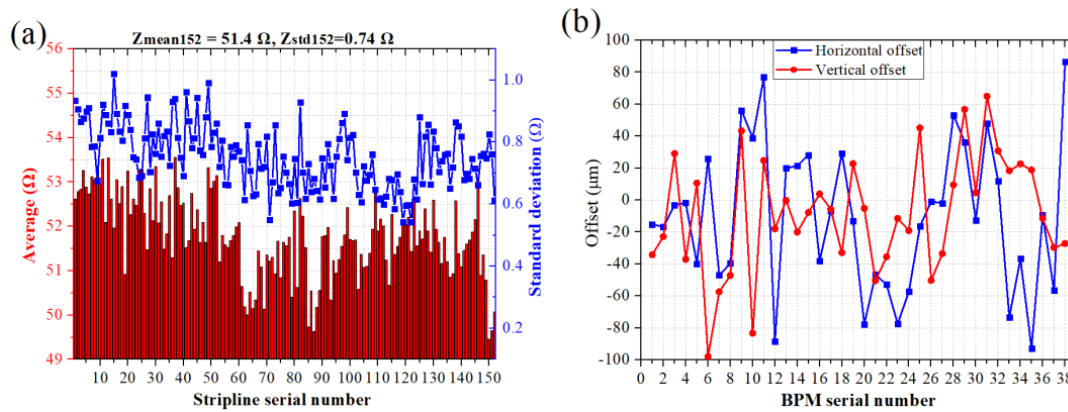


Figure 2. (a) Characteristic impedance values of 152 stripline electrodes, where average and standard deviation were calculated using 1600 points, which corresponded to 0.5–1.2 ns in Figure 1c. (b) The position measurement offsets caused by the impedance difference between the electrodes.

The next step was to analyze the impact of machining errors on the measurement. The stripline electrodes are orthogonal, and the following two-electrode algorithm was used for the beam position measurement [14]:

$$x = k_x \times \frac{U_R - U_L}{U_R + U_L}, y = k_y \times \frac{U_U - U_D}{U_U + U_D}, k_x = k_y \approx r_{\text{in}} / 2 = 7.5 \text{ mm}, \quad (1)$$

where U_L , U_R , U_U , and U_D are the signal strengths of the left, right, up, and down electrodes, respectively; k is the sensitivity coefficient. The signal strength of a BPM could be characterized by the transfer impedance. The output signal (frequency domain), beam current intensity, and transfer impedance satisfy the following [15]:

$$U_{\text{output}}(\omega) = I_{\text{beam}} \omega \times Z_t(\omega), \quad (2)$$

where $Z_t(\omega)$ is the transfer impedance, which satisfies the following [15]:

$$Z_t(\omega) = Z_{\text{strip}} \cdot \frac{\alpha}{2\pi} e^{-\frac{\omega^2 v_L^2}{2}} \sin\left(\frac{\omega L_{\text{strip}}}{c}\right) \cdot e^{i\left(\frac{\pi}{2} - \frac{\omega L_{\text{strip}}}{c}\right)}. \quad (3)$$

Here, Z_{strip} , L_{strip} , and α are the characteristic impedance, longitudinal length, and cover angle of the stripline, respectively; and c is the speed of light. Ignoring the impedance matching error with the cable, the signal strength can be approximated using the characteristic impedance. The x_{offset} value caused by the inconsistency between electrodes A and C can be evaluated by replacing U_R with Z_{stripR} and U_L with Z_{stripL} in Equation (2). The offset results of 38 stripline BPMs are shown in Figure 2b, where y_{offset} could be obtained using the characteristic impedance difference between electrodes B and D. The deviations caused by electrode differences were smaller than $100 \mu\text{m}$, which is acceptable for the accuracy requirements.

3. Button Measurement and Sorting

Compared to the stripline BPMs, there are a larger number of button-type BPMs, and their accuracy requirements are higher, as listed in Tables 1 and 2. Figure 3a,b show a

mechanical drawing and prototype of a BPM with RF shielding bellows. The transfer impedance of the button BPM can be found as follows [16,17]:

$$Z_t = \frac{r_b^2 R_0 \omega}{2bc(1 + R_0^2 C_b^2 \omega^2)} (R_0 C_b \omega + j), \tag{4}$$

where r_b and C_b are the radius and capacitance of the button, respectively. R_0 is the load impedance of the output circuit. b is the distance from the center of the pipe to the button, and c is the speed of light.

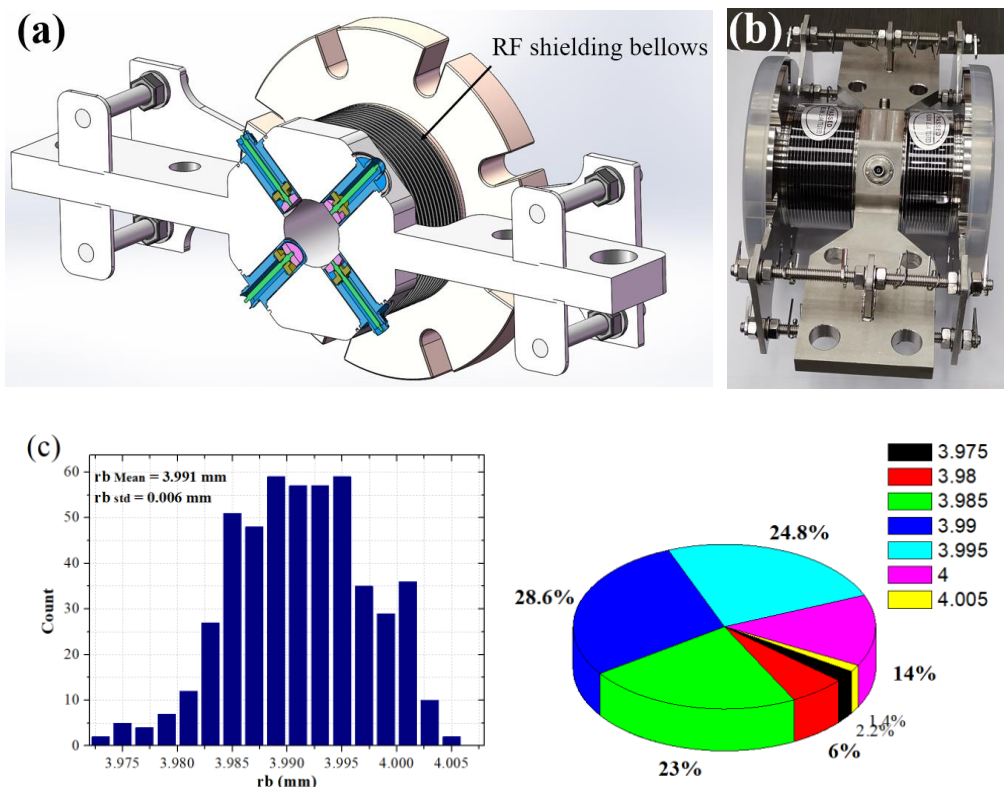


Figure 3. (a) BPM with RF shielding bellows for HEPS. (b) The BPM prototype. (c) Radius deviation for 500 buttons.

A button electrode and ultra-high vacuum (UHV) RF feedthrough were combined into a pickup, which was welded on a vacuum chamber with two RF shielding bellows on both sides. Any defect in the button requires a complete chamber replacement. For this reason, a thorough verification of the feedthrough quality is mandatory. Three important parameters, r_b , C_b , and b , are directly connected to the button output signal according to Equation (4). The radius measurement results for 500 buttons are shown in Figure 3c. The STD of the radius was only 6 μm , and more than 76% (380 pieces) of the feedthroughs were concentrated at 3.990 ± 0.005 mm. A radius deviation of ± 5 μm induces a position deviation of ± 5 μm according to Equation (4), assuming that the other parameters are kept constant ($C_b = 2.4$ pF, $b = 11$ mm).

To reduce the offsets caused by the difference in the four feedthroughs, the feedthroughs were sorted and classified according to the measured values of b and C_b . The position of a button electrode was determined by the machining accuracy of the feedthrough and BPM block. The standard distance between the button and welding point was 20 mm, as shown in Figure 4a. The measured values and distribution of the 500 buttons are shown in Figure 4b. The maximum allowable deviation between four buttons during sorting was 30 μm . Better machining accuracy for the BPM block was easy to implement before

welding. Two measures were used to further improve the accuracy: every BPM block was specially machined according to the average dimensions of the four feedthroughs, and the difference in deformation due to different argon-arc welding currents was also studied. Based on experience, there will be 30–50 μm of shrinkage caused by heat during welding. The distance between the welded button and center of the pipe was measured using a three-coordinate measuring instrument, and the results are shown in Figure 5a. Similar to the stripline BPMs, the offsets can be evaluated as follows:

$$offset\ x = k_x \times \frac{U_a+U_d-U_b-U_c}{U_a+U_b+U_c+U_d},\ offset\ y = k_y \times \frac{U_a+U_b-U_c-U_d}{U_a+U_b+U_c+U_d}, \tag{5}$$

where $k_x = k_y = 11\text{ mm}$ for the booster, and $k_x = k_y = 8\text{ mm}$ for the storage ring. U_a is the signal strength of electrode A and can be replaced with Z_t of electrode A. The offsets caused by the Δb values of the four electrodes according to Equation (5) are shown in Figure 5b. The STD of b for 280 buttons was 43 μm, and the STD values of the horizontal and vertical offsets for 70 BPMs were 7 and 11 μm, respectively.

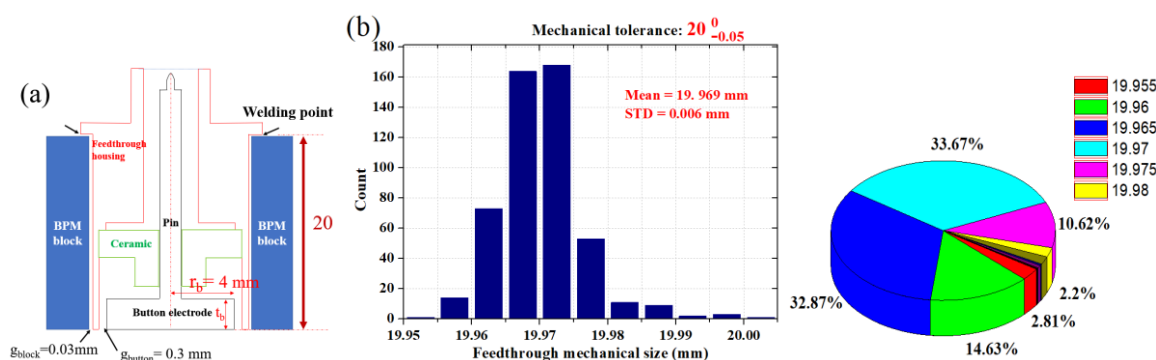


Figure 4. (a) Schematic of feedthrough with button showing mechanical parameters. (b) Mechanical size deviation for 500 buttons.

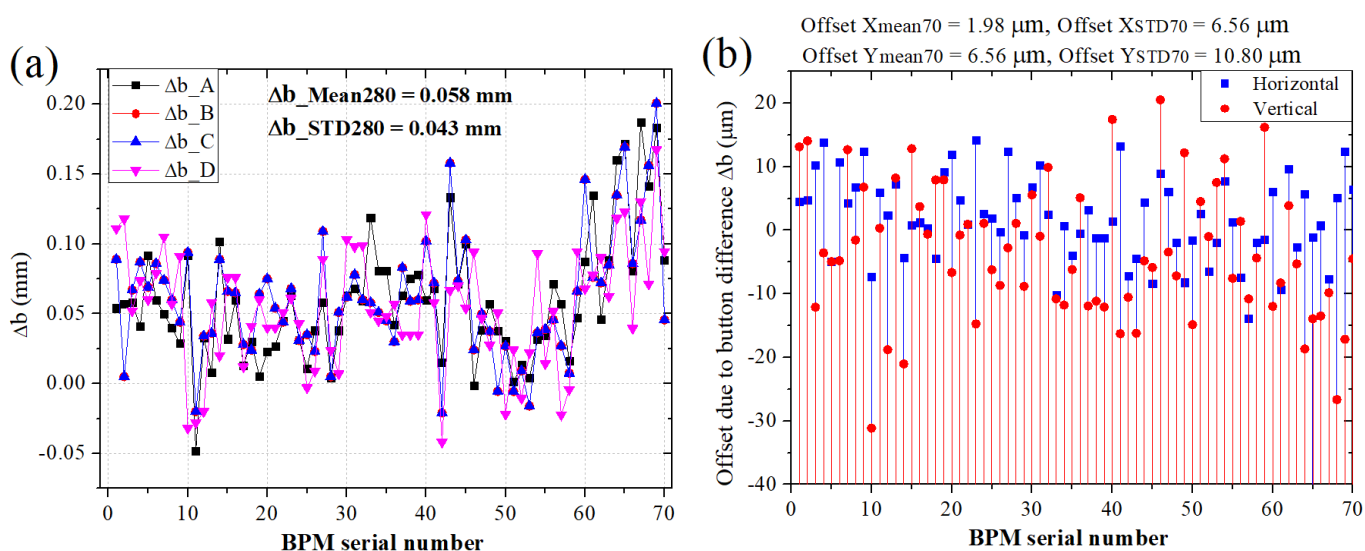


Figure 5. (a) Distance difference from center of BPM pipe to button for 70 BPMs. (b) Horizontal and vertical offsets due to Δb .

Similar to the mechanical size, the button capacitances were similar and sorted into groups. The maximum capacitance deviation allowed between the four electrodes was 0.03 pF, and the offsets corresponding to 0.03 pF were 5 and 7 μm for the booster and

storage rings, respectively. Considering the button capacitance changes in the mounted configuration owing to fringe fields, we measured the button capacitance twice. The results for the 280 buttons before and after welding are shown in Figure 6a. The offsets caused by the ΔC_b values are shown in Figure 6b,c, and the STD values of the 70 BPMs were 8 and 7 μm in the horizontal and vertical directions, respectively. After welding, the STD values were 12 and 16 μm , respectively, because of the dual effects of C_b and b .

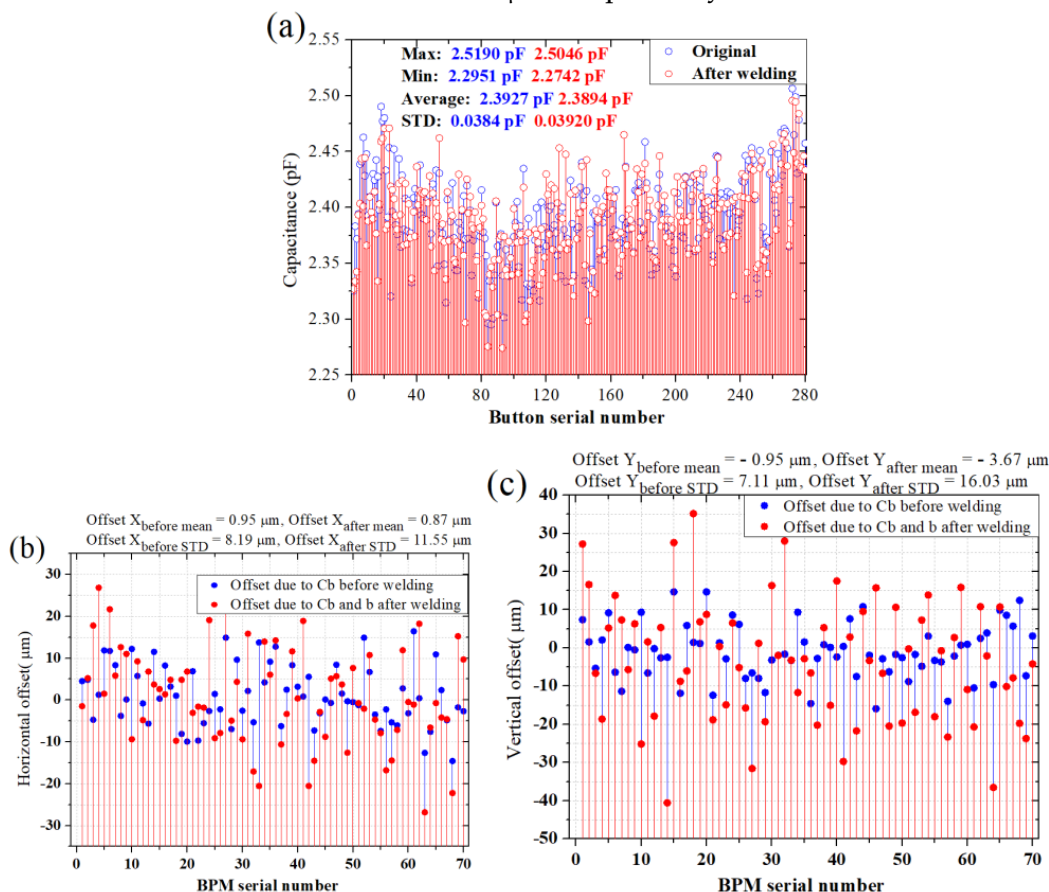


Figure 6. (a) Original and welded button capacitance values measured by TDR. (b,c) Horizontal and vertical offsets due to ΔC_b and Δb .

In addition to the above tests, we also performed other tests on the feedthroughs, including hermeticity, DC withstand voltage, and permeability tests.

4. BPM Electro-Mechanical Offset Measurements

Although the beam-based alignment (BBA) technique corrects the electromagnetic offset (the magnetic and electrical center, \vec{QE}) with very high accuracy [18,19]. We needed to control it with a level of $<200 \mu\text{m}$ (RMS value for all the BPMs in the storage ring) on day one. As shown in Figure 7a, the three centers Q, M and E satisfy the equation:

$$\vec{QE} = \vec{QM} + \vec{ME}, \tag{6}$$

where Q and M are the centers of the quadrupole and the pipe. Because of the large nonlinear effects on the beam dynamics of the HEPS, the tolerances for the misalignment and field error of the quadrupole were stringent. One feature of the HEPS is that the position of the sextupole can be adjusted online [20]. Although it is helpful to measure \vec{QE} using a stretched wire, this requires significant alignment efforts [21]. It is more common to

measure electro-mechanical offset \vec{ME} and left \vec{QM} in the alignment procedure. The QM requirements of \vec{QM} for the HEPS were $\pm 30 \mu\text{m}$ [22].

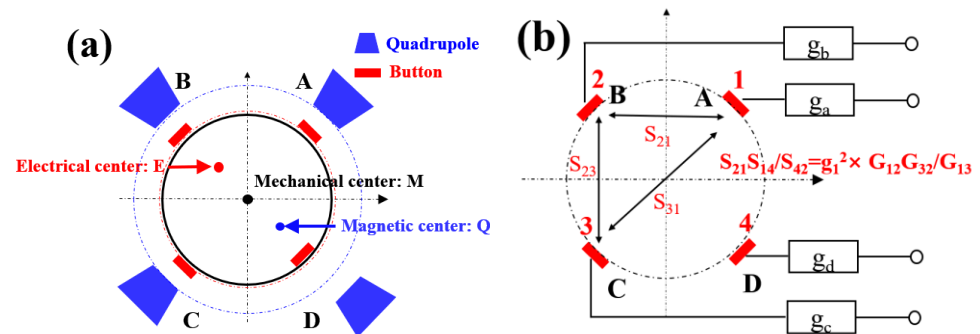


Figure 7. (a) Schematic of magnetic-mechanical offset and electro-mechanical offset where quadrupole A and button C deviate from ideal positions. (b) Schematic of the offset determined by Lambertson method, where g_i represents the gain associated with button i .

Figure 7a shows the electric and magnetic centers when quadrupole D and button D deviate from their ideal positions. We measured the electro-mechanical offset using two different methods. The first was the so-called Lambertson method [23], which is based on the scattering parameters (S-parameters) for four buttons of a BPM measured by a network vector analyzer (NVA). The transmission efficiency between buttons i and j was denoted by S_{ij} . The process was repeated on all the buttons, and an S-parameter matrix was obtained. Ideally, the transmission should be symmetric ($S_{12} = S_{21}$, $S_{13} = S_{31}$...). The gain factor, g_i , of each electrode can be determined by the S-parameters, and the ratios between the gain factors provide \vec{ME} , which results in the deviation of the four channels depending on the feedthrough, BPM block, and welding processing. As shown in Figure 7b, the signals satisfy the following equation [23,24]:

$$V_{ij} = 2 \times 50 \times G_{ij} g_i g_j, \quad (7)$$

where $G_{ij} = G_{ji}$ are the coupling coefficients.

g_i can be obtained by V_{ij} ; for example, for g_1 ,

$$2 \times 50 \times g_1^2 = \frac{V_{21} V_{14}}{V_{42}} \times \frac{G_{13}}{G_{12} G_{23}} = \frac{V_{21} V_{31}}{V_{32}} \times \frac{G_{23}}{G_{12} G_{13}} = \frac{V_{41} V_{31}}{V_{43}} \times \frac{G_{12}}{G_{23} G_{13}}, \quad (8)$$

and three similar triplet sets can be found for $g_{2,3,4}$. \vec{ME} can be calculated as follows [23–25]:

$$x_{\text{offset}} = k_x \times \frac{g_2 - g_1 - g_4 + g_3}{g_1 + g_2 + g_3 + g_4}, \quad y_{\text{offset}} = k_y \times \frac{g_1 + g_2 - g_3 - g_4}{g_1 + g_2 + g_3 + g_4}. \quad (9)$$

Figure 8a shows the S-parameter results in the frequency range of 300 kHz–20 GHz, where the resonance peaks are the trapped modes due to the button feedthrough. The goal of these measurements was to improve the accuracy of the S-parameters less than -70 dB. There were several steps. First, error correction was applied to the VNA measurements using a calibration procedure. Second, a higher input power level (15 dBm), narrow IF bandwidth (100 Hz), and multiple averages (1000 points) for the VNA were used. Third, low-noise coaxial cables were used, and the measurement environment, including the temperature and humidity, was the same as that of the accelerator tunnel. The processing frequency of the BPM readout electronics was 500 MHz, and a 500 MHz \pm 10 MHz electronic filter was used. We only considered the transmission at this frequency. The S-parameter measurement results are shown in Figure 8b. Table 4 lists the offset results for BPM prototypes manufactured by different manufacturers. The STD and repeat precision

had values of several micrometers. Manufacturers 1 and 4 are responsible for the production of the storage rings and booster BPMs for the HEPS, respectively.

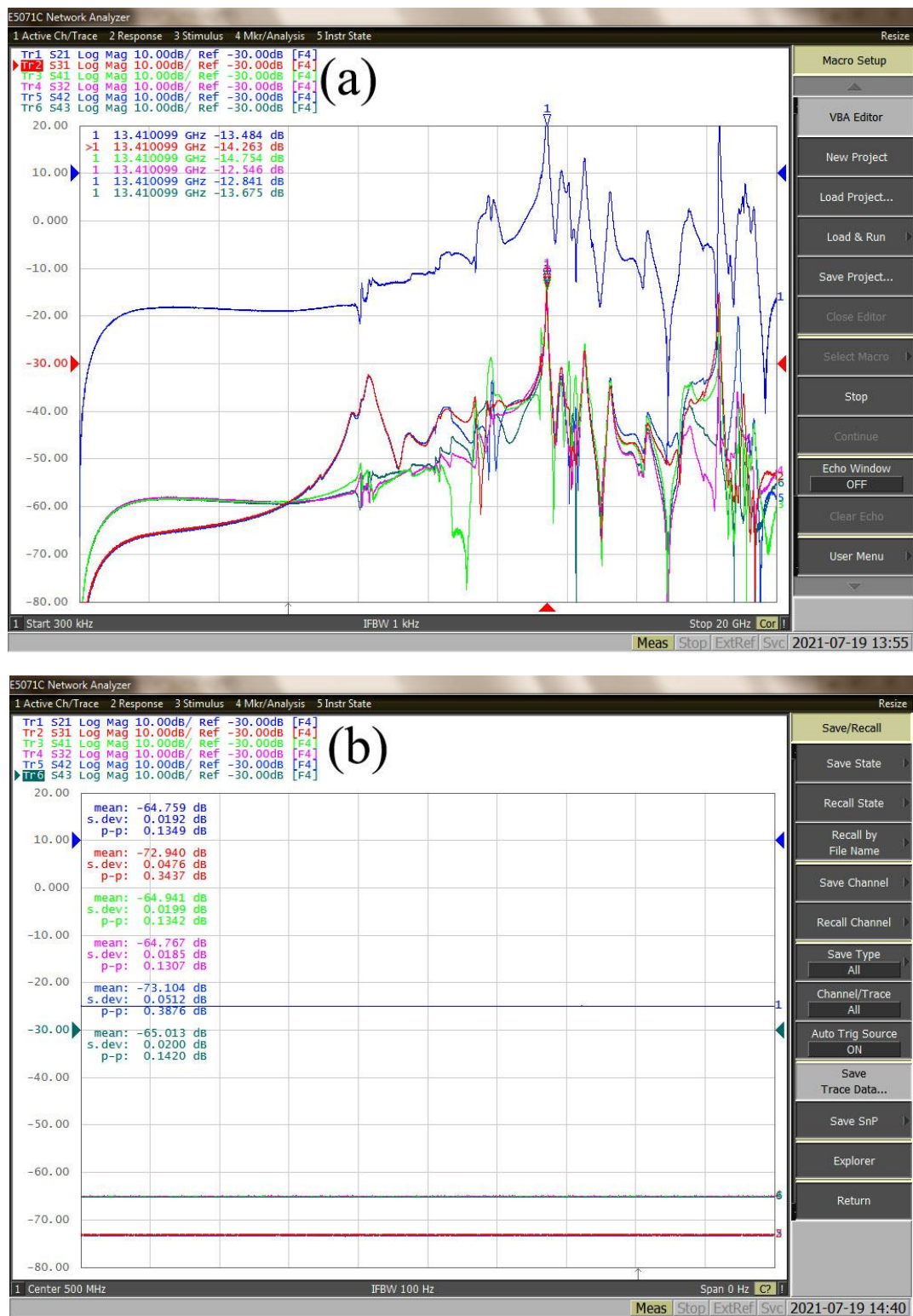
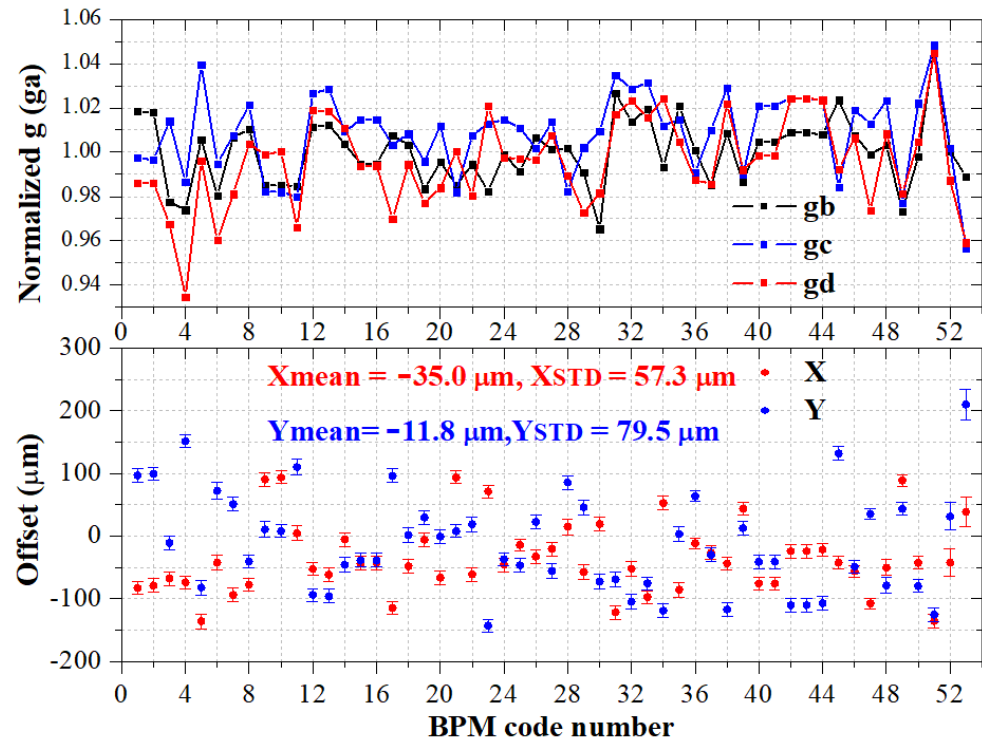


Figure 8. (a) S-parameters in frequency range of 300 kHz–20 GHz with IF bandwidth of 1 kHz. (b) S-parameters in a CW sweep mode at a frequency of 500 MHz, with an IF bandwidth of 100 Hz.

Table 4. Electro-mechanical offset of HEPS BPM measured by Lambertson method (in μm).

BPM			VNA 1		VNA 2	
			Day 1-1st	Day 1-remade	Day 2	Day 3
Store Ring $k_x = k_y = 8 \text{ mm}$	Manufacturer 1	x_{offset}/STD	37.6/6.7	36.7/6.9	35.6/6.4	33.5/8.5
		y_{offset}/STD	48.3/7.3	49.6/6.3	58.3/6.7	53.0/7.2
	Manufacturer 2	x_{offset}/STD	−30.2/6.7	/	/	−27.2/7.3
		y_{offset}/STD	−68.2/6.6	/	/	69.0/7.2
	Manufacturer 3	x_{offset}/STD	435.3/8.3	/	439.3/8.1	/
		y_{offset}/STD	−468.5/8.6	/	−449.5/8.7	/
Booster $k_x = k_y = 11 \text{ mm}$	Manufacturer 4	x_{offset}/STD	84.5/23.1	/	83.2/22.6	85.6/17.8
		y_{offset}/STD	165.3/23.5	/	170.6/21.5	16.1/17.7

The electro-mechanical offset of a BPM can be determined by the unequal electrical behavior of the feedthroughs, asymmetry of the BPM block, and positioning deviation of the feedthroughs due to the welding process. Figure 9 shows the electromechanical offset results for 53 BPMs, where the error bar is the STD of 1000 points.

**Figure 9.** Electro-mechanical offset distribution for 53 BPMs.

5. BPM Calibration Using Stretched Wire

As shown in Equation (4), the signal of BPM pick up is determined by r_b , b and C_b . Equations (10) and (11) show the differences for two electrodes and four electrodes, respectively:

$$X_{\text{raw}} = \frac{U_R - U_L}{U_R + U_L}, \quad Y_{\text{raw}} = \frac{U_U - U_D}{U_U + U_D} \quad (10)$$

$$X_{\text{raw}} = \frac{U_a - U_b + U_c - U_d}{U_a + U_b + U_c + U_d}, \quad Y_{\text{raw}} = \frac{U_a + U_b - U_c - U_d}{U_a + U_b + U_c + U_d}. \quad (11)$$

where U_i is the signal of button i . The position of the beam can be estimated using a polynomial of $(X_{\text{raw}}, Y_{\text{raw}})$ as follows [4,26–28]:

$$x = \sum_{i=0}^n \sum_{j=0}^i A_{i-j,j} X_{\text{raw}}^{i-j} Y_{\text{raw}}^j, \quad y = \sum_{i=0}^n \sum_{j=0}^i B_{i-j,j} X_{\text{raw}}^{i-j} Y_{\text{raw}}^j, \quad (12)$$

where $A_{i-j,j}$ and $B_{i-j,j}$ are the horizontal and vertical polynomial coefficients, respectively; and n is the polynomial order. $A_{0,0}$ and $B_{0,0}$ are the offsets; $A_{1,0}$ and $B_{0,1}$ are the BPM’s sensitivity constants in the horizontal and vertical planes, respectively; and $A_{0,1}$, $B_{1,0}$ are the related to the coupling coefficients between the horizontal and vertical planes. The values of $A_{i-j,j}$ and $B_{i-j,j}$ in Equation (12) were determined by the least squares method to fit X_{raw} and Y_{raw} .

A BPM is usually calibrated with a wire installation. We changed the position of the wire stepwise and recorded X_{raw} and Y_{raw} and $A_{i-j,j}$ and $B_{i-j,j}$ were calculated [29]. Impedance matching between the input coax cable and stretched wire or antenna was performed with a Klopfenstein taper to reduce reflection; and the rigid marble platform was replaced with an active vibration platform. The BPMs were calibrated with two different origins: the mechanical center, which was determined using four fiducial target balls, and the electrical center, where $U_a = U_b = U_c = U_d$. A complex alignment process was required to improve the repeat positioning accuracy (both the wire and BPM) to 10 μm . The alignment resources were concentrated on the installation of the HEPS accelerator, and a few BPMs were selected and calibrated based on the mechanical center, which was used to evaluate the precision of the machining and welding. The calibration of most of the BPMs was based on the electrical center, which was much easier.

5.1. Calibration Based on Mechanical Center

If a BPM is strictly aligned with a stretched wire, that is, the mechanical center is selected as the origin of the calibration, offset \vec{QE} can be obtained. The offsets measured by two methods are listed in Table 5. The difference between the two results is below 50 microns.

Table 5. Results of offset measurement using stretched wire and Lambertson method.

	Stretched Wire (μm)		Lambertson (μm)	
	Offset x	Offset y	Offset x	Offset y
Storage Ring BPM-01 ($k = 8 \text{ mm}$)	−10	−70	$−52.1 \pm 2.8$	$−34.1 \pm 2.8$
Storage Ring BPM-02 ($k = 8 \text{ mm}$)	−30	10	$−78.5 \pm 2.9$	$−10.0 \pm 2.9$
Storage Ring BPM-03 ($k = 8 \text{ mm}$)	−160	−110	$−196.1 \pm 2.9$	$−74.2 \pm 2.9$
Booster BPM-77 ($k = 11 \text{ mm}$)	−105	−110	$−135.7 \pm 9.0$	$−125.8 \pm 9.2$

5.2. Calibration Based on Electrical Center

5.2.1. Origin and Fitting Coefficients

Before performing the calibration based on the electrical center, the offset, \vec{QE} , of each BPM was checked to confirm that it was smaller than 300 μm . Otherwise, the BPM was treated as an unqualified product. Table 6 lists the linear fitting results for a booster BPM based on three different origins (P_0 , P_1 , and P_2), satisfying $\left| \vec{P_0P_1} \right| = \left| \vec{P_0P_2} \right| = 200 \pm 1 \mu\text{m}$. A precision of $\pm 1 \mu\text{m}$ was achieved using a mobile platform with a grating. The position sensitivity coefficient, k , and coupling coefficient are independent of the origin if the offset is small.

Table 6. Linear calibration results are based on different origins.

Parameters	Offset x (μm)	Offset y (μm)	k_x (mm)	k_y (mm)	Coupling x to y (mrad)	Coupling y to x (mrad)
Symbol in Equation (2)	$A_{0,0}$	$B_{0,0}$	$A_{1,0}$	$B_{0,1}$	$A_{0,1}/B_{0,1}$	$B_{1,0}/A_{1,0}$
The origin P_0 : electrical center $x_0 = y_0 = 0$	-1.3	20.9	11.190	11.339	-8.9	-11.0
The origin P_1 : $x_0 = -200 \mu\text{m}, y_0 = 0$	-195.7	20.0	11.189	11.333	-8.4	-10.4
The origin P_2 : $x_0 = 0, y_0 = -200 \mu\text{m}$	-4.7	-180.2	11.191	11.338	-8.6	-10.9

5.2.2. Calibration Range and Fitting Errors

To obtain fitting coefficients with a higher accuracy and smaller fitting error, $\sqrt{(x - x_{fit})^2 + (y - y_{fit})^2}$, where $x(y)$ and $x_{fit}(y_{fit})$ are the beam positions (the real positions of the stretched wire) given by Equation (6) (measured beam position), the relationship between the calibration range and fitting error was studied. In the initial preliminary commissioning phase and user’s operation phase, the beam position (orbit) may be quite different, whereas the latter will be much smaller after optical correction. The signal strengths on the pickup were also significantly different for centric and off-centered beams. Assuming that the signal strength is -20 dBm when the beam is in the center, discarding the automatic gain adjustment function, when the beam moves along the diagonal line formed by buttons A and C, the signal strength changes of the four electrodes are shown in Figure 10. The slopes of A, C and B(D) were approximately 1.6, -1.6 and -0.4 dB/mm in the central area, respectively.

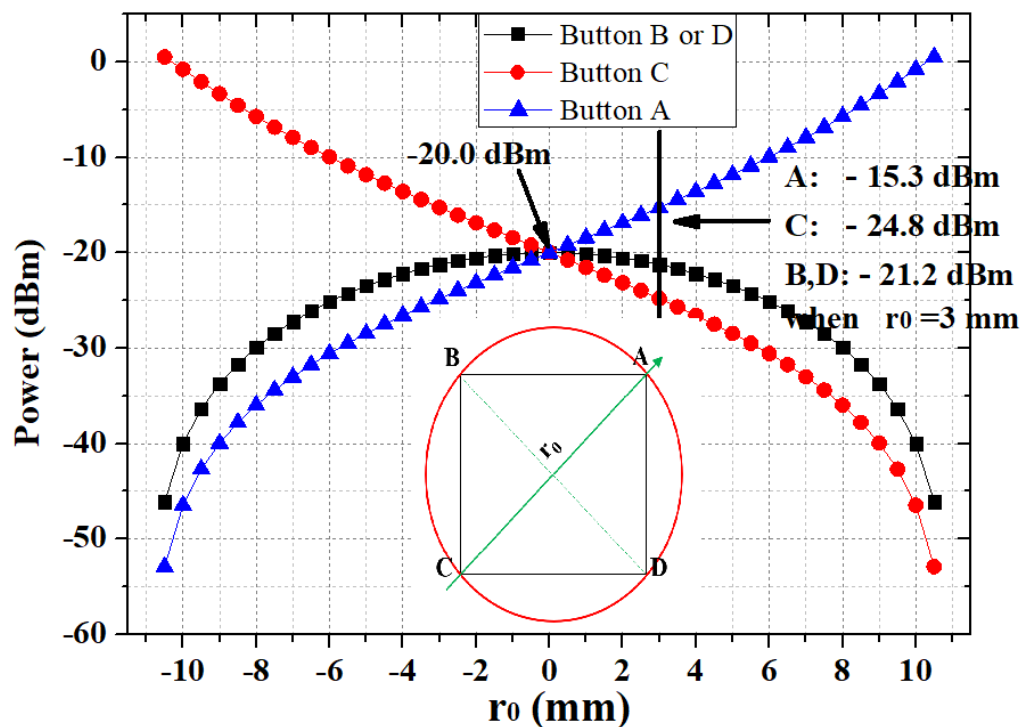


Figure 10. Output signal strength on HEPS storage ring BPM for off-axis beam, assuming beam moves along diagonal line (from button C to button A).

If the calibration range has been determined, the results in Figure 10 can assist in evaluating whether the ADC will be saturated based on the ADC reading when the stretched wire is in the center of the pipe when the calibration begins. Figure 11a shows the linear

fitting results (x_{fit} and y_{fit}) of a typical HEPS storage ring BPM with a range of ± 6 mm in 1 mm steps. The distribution of the fitting error, $\sqrt{(x - x_{\text{fit}})^2 + (y - y_{\text{fit}})^2}$ is shown in Figure 11b, where the error is smaller in the center region than in the edge area. Figure 11c shows the average values of $\sqrt{(x - x_{\text{fit}})^2 + (y - y_{\text{fit}})^2}$ with steps of 0.25 mm and a different fitting order, n . When x/y changes from 0.25 to 7.00 mm, the total number of scan points is 9, 25, 49, 81, ..., 3249, and the time consumption of the calibration process increases exponentially. As shown in Figure 11c, the errors first decrease because the increase in the number of scan points reduces the accidental errors and then increases because of the nonlinear response of the BPMs. When the scan range increased, the error of the first-order (second-order) fitting increased rapidly, whereas the error of the high-order fitting increased much more slowly. Figure 11d shows the linear fitting results with different calibration ranges, indicating that a precise sensitivity constant, k ($A_{1,0}$), could only be determined within a reasonable calibration range.

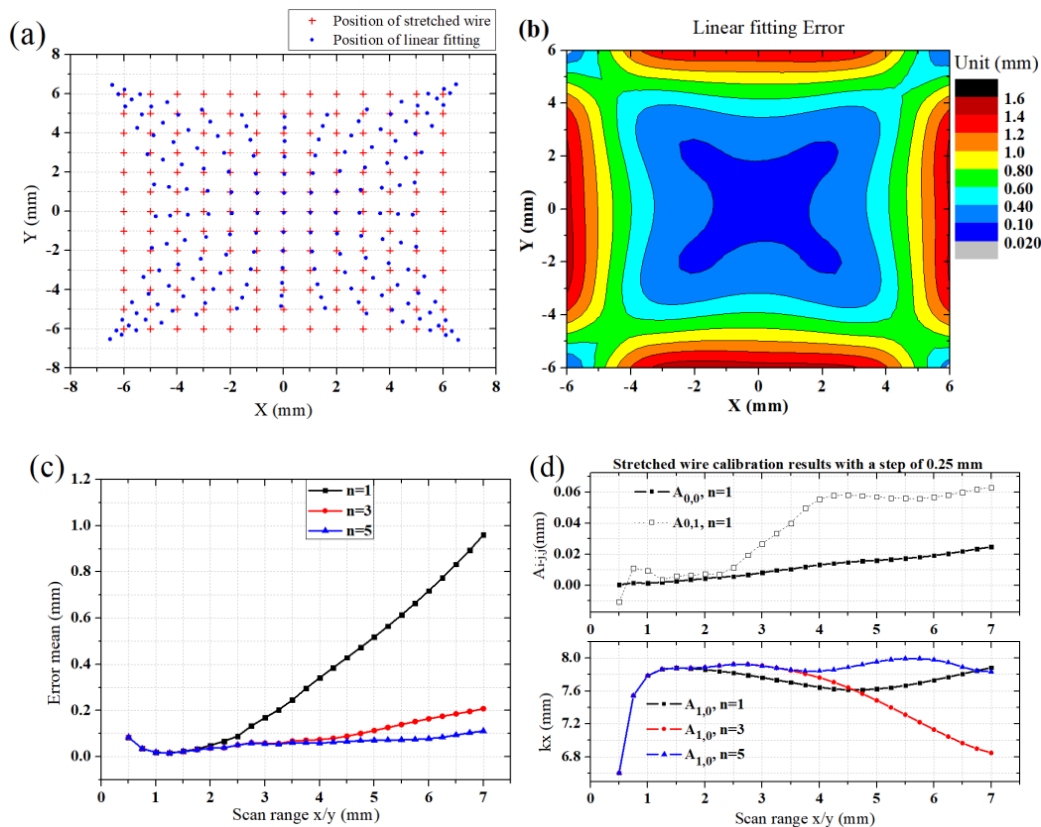


Figure 11. (a) Calibration map of HEPS BPM using stretched wire, with wire position determined by linear fitting of X_{raw} and Y_{raw} . (b) Fitting error $\sqrt{(x - x_{\text{fit}})^2 + (y - y_{\text{fit}})^2}$ distribution in range of ± 6 mm with steps of 1 mm. (c) Average value of fitting error and (d) fitting results for $A_{i-j,j}$ and $B_{i-j,j}$.

5.2.3. Calibration Order n and Fitting Errors

As shown in Figure 11c, the errors for the high-order fitting were much smaller than those for linear fitting, especially in a larger calibration range. To eliminate the impact of accidental errors on the BPM manufacturing process, we repeated the calibration procedure using the CST simulation in a range of ± 6 mm with steps of 0.5 mm. The simulation showed that the errors were the same for $n = 1$ and 2, as well as for $n = 3$ and 4, $n = 5$ and 6, and $n = 7$ and 8. The fitting sensitivity coefficient, k , was also exactly the same ($k_x^{n=1} = k_y^{n=1} = k_x^{n=2} = k_y^{n=2}$). Figure 12 shows that the fitting error distributions for n

were 1, 3, 5, and 7. With a higher fitting order, the errors were much smaller, but there were more calibration coefficients. The number, $A_{i-j,j}(B_{i-j,j})$, and fitting order n satisfied

$$N_{\text{fitting}} = n \times \frac{n + 3}{2} + 1. \tag{13}$$

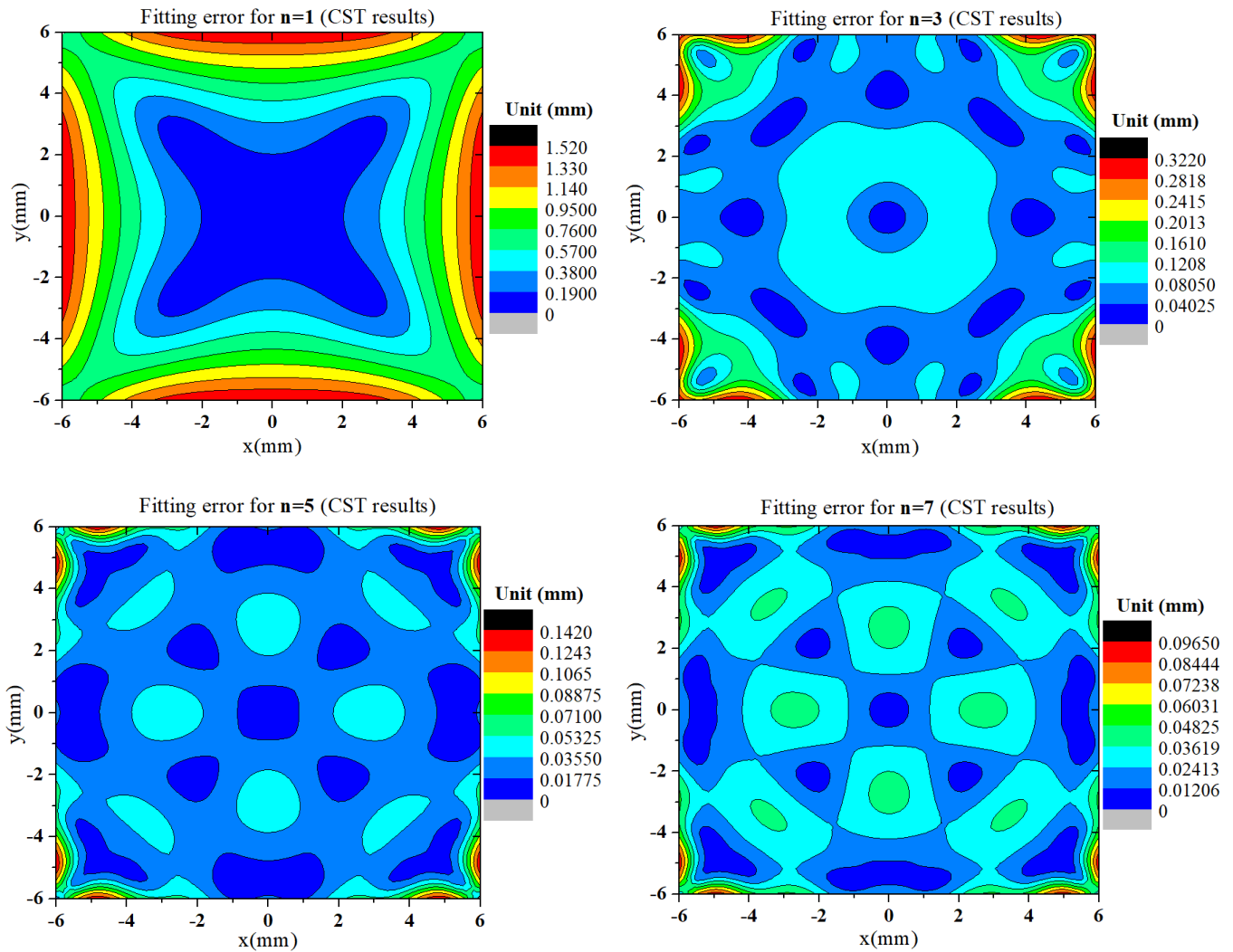


Figure 12. Fitting error distributions for different values of n (CST results).

The calibration parameters used for the HEPS BPM are listed in Table 7.

Table 7. Calibration parameters for HEPS BPM.

		Calibration Range (mm)	Calibration Step (mm)	Calibration Order n	Number of $A_{i-j,j} (B_{i-j,j})$	Expected Error (mm)
Storage ring BPM	Normal operation phase	$x = y = \pm 1$	0.05	5	21 (21)	<0.05
	Commissioning phase	$x = y = \pm 6$	0.25	7	36 (36)	<0.1
Booster BPM 36×30 mm		$x = y = \pm 8$	0.5	5	21 (21)	<0.15
Booster BPM 36×52 mm		$x = y = \pm 10$	0.5	5	21 (21)	<0.15

5.2.4. Calibration Results for Booster BPM

All of the booster BPMs were manufactured, and we calibrated most of them. Figure 13a–c show the linear calibration results for $A_{0,0}(B_{0,0})$, $A_{1,0}(B_{0,1})$, and $A_{0,1}(B_{1,0})$, respectively. The origin, where the electrical center was located, was determined by moving the BPM (the stretched wire remained still) to make the position reading given by the BPM read-out electronics $< \pm 5 \mu\text{m}$. The offset results for both plans were in the range of $\pm 5 \mu\text{m}$, and the values of k_x and k_y were 11.18 and 11.33 mm, respectively. The coupling was also on the order of $10 \mu\text{m}$. The statistical results for the 62 BPMs are listed in Table 8. The results in Table 8 show the comprehensive consistency of the BPM batch processing and the accuracy of the calibration system. We did not find batch calibration data from other laboratories in the open literature, but the statistical data for the button capacitance used in the HEPS are at the same level as SIRIUS in LNL [30]. The electrical center offset measured by the Lambertson method showed that the consistency of the HEPS BPM was better than that of ALBA [31].

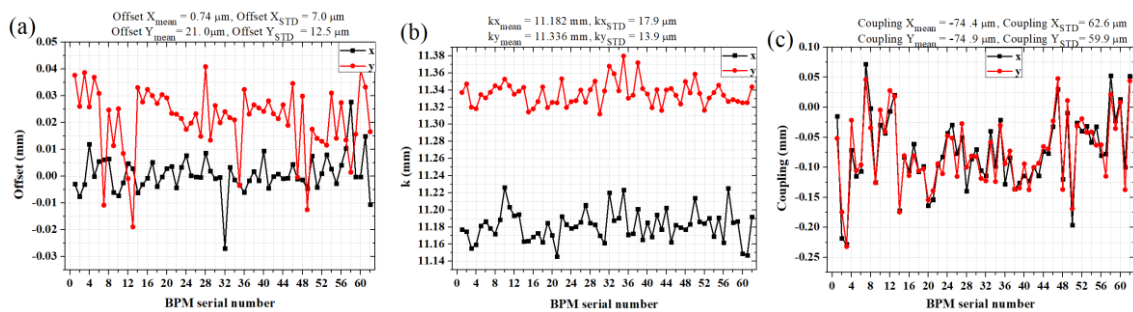


Figure 13. Fitting results for 62 BPMs, where $n = 1$, scan range = ± 6 mm, and scan step = 0.5 mm: (a) offset, (b) k and (c) coupling coefficient.

Table 8. Statistics of BPM Measurements.

Measurement Object	Parameters	Standard Value	Amount	Average	STD
Stripline	Characteristic impedance	50 Ω	152	51 Ω	0.7 Ω
	Radius	4 mm	500	3.991 mm	6 μm
Feedthrough with button	Distance between the button and welding point	20 mm	500	19.969	6 μm
	Capacitance	2.2 pF (CST)	500	2.385 pF	0.044 pF
	Permeability	<1.03	380	1.112	0.022
	Permeability	<1.03	230	1.019	0.003
	Distance between the button and pipe axis	16.098 mm	280	16.156 mm	43 μm
Booster button-type BPM	Electro-mechanical offset X/Y	0	53	-35/-12 μm	57/80 μm
	Calibration coefficient Offset X/Y	<1 μm (CST)	62	1/21 μm	7/13 μm
	Calibration coefficient k X/Y	11.406 mm/11.597 mm (CST)	62	11.182/11.336 mm	20/14 μm
	Calibration coefficient $A_{0,1}/B_{1,0}$	<1 μm (CST)	62	-74/-75 μm	63/60 μm

6. Other Measurements and Summary of Results

In addition to the measurements mentioned above, other parameters were also checked, including the magnetic permeability, hermeticity, and button gap. The magnetic permeability of the first batch of feedthroughs did not satisfy the requirements. After the production process was improved, the magnetic permeability was approximately 1.02, which was the same as that required for the vacuum pipe. Because the size of the feedthrough is small and the magnetic permeability of most feedthroughs is less than 1.03, we decided to accept the feedthroughs. The magnetic permeability measurement results for the two batches of feedthroughs before and after the production process improvement are shown in Figure 14. Some of the unqualified feedthroughs were used for prototype and booster BPM production, and the rest were abandoned. The statistics of magnetic permeability and other previous test results are summarized in Table 8, which can be used as a reference for other accelerator projects.

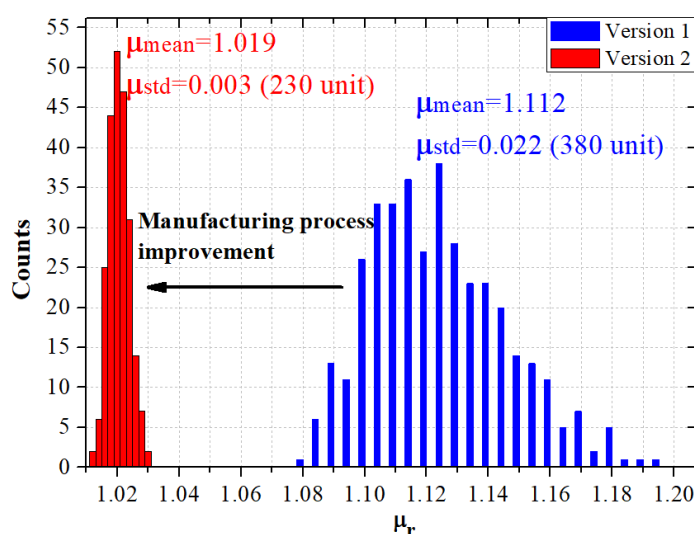


Figure 14. Magnetic permeability measurement results for two versions of feedthroughs, which consisted of 380 and 230 units.

7. Conclusions

There are more than 700 BPMs in the HEPS, involving 3000 feedthroughs. The physical and mechanical design of the feedthroughs and BPMs has been completed, and the project has now entered the batch processing stage. We carried out various characterizations of more than 1000 feedthroughs and more than 100 of the BPMs produced, and the results showed that most of these feedthroughs and BPMs meet our requirements. The average value for the characteristic impedance of the 152 BPM stripline electrodes was 51.0Ω , with a standard deviation of 0.7Ω . The average values for the electro-mechanical offsets of 53 booster BPMs measured by Lambertson method in the horizontal and vertical plane were -35 and $-12 \mu\text{m}$, respectively, and the STD of the offsets were 57 and $80 \mu\text{m}$, respectively. The 62 booster BPMs were calibrated based on the electric center with a stretched wire, and the average values of the coefficients in the horizontal plane were $1 \mu\text{m}$, 11.182 mm , $-74 \mu\text{m}$, with STD values of 7 , 20 , and $63 \mu\text{m}$, respectively. The average values of the coefficients in the vertical plane were $21 \mu\text{m}$, 11.336 mm , and $-75 \mu\text{m}$, with STD values of 13 , 14 , and $63 \mu\text{m}$, respectively. The symmetry of BPM pickup is crucial to the beam accumulation during the first turn, two measures are used to help improve it. First, to sort feedthroughs according to the capacitance. Second, the processing size of each BPM block is matched one by one according to the mechanical size of the feedthrough. The batch production of the HEPS BPMs is steadily progressing. Although some of the BPMs and feedthroughs have not been completed, the measured data confirmed that the production technology and quality control of the relevant manufacturers are in line with the requirements of the HEPS.

Author Contributions: Conceptualization, J.H. and Y.S.; methodology, J.H.; validation, Y.L. and Y.D.; resources, H.M. and X.W.; writing—review and editing, J.H. and Y.S.; project administration, J.C.; funding acquisition, Y.S. and J.Y. All authors have read and agreed to the published version of the manuscript.

Funding: This research was funded by the Youth Innovation Promotion Association CAS (No. 2019013 and Y202005) and the National Natural Science Foundation of China (No. 11975254).

Data Availability Statement: The data that support the findings of this study are available on request from the corresponding author, [J. He, hejun@ihep.ac.cn], upon reasonable request.

Acknowledgments: The authors would like to thank Daheng Ji and Yi Jiao for helpful discussions.

Conflicts of Interest: The authors declare no conflict of interest. The funders had no role in the design of the study; in the collection, analyses, or interpretation of data; in the writing of the manuscript, or in the decision to publish the results.

References

1. Jiao, Y.; Xu, G.; Cui, X.H.; Duan, Z.; Guo, Y.Y.; He, P.; Ji, D.H.; Li, J.Y.; Li, X.Y.; Meng, C.; et al. The HEPS project. *J. Synchrotron Radiat.* **2018**, *25*, 1611–1618. [[CrossRef](#)] [[PubMed](#)]
2. Jiao, Y.; Chen, F.; He, P.; Li, C.; Li, J.; Qin, Q.; Qu, H.; Wan, J.; Wang, J.; Xu, G. Modification and optimization of the storage ring lattice of the High Energy Photon Source. *Radiat. Detect. Technol. Methods* **2020**, *4*, 415–424. [[CrossRef](#)]
3. He, J.; Sui, Y.; Li, Y.; Ma, H.; Du, Y.; Zhao, Y.; Zhang, W.; Wei, S.; Xu, T.; Yue, J.; et al. Beam position monitor design for the High Energy Photon Source. *Meas. Sci. Technol.* **2022**, *33*, 115106. [[CrossRef](#)]
4. He, J.; Sui, Y.-F.; Li, Y.; Tang, X.-H.; Wang, L.; Liu, F.; Liu, Z.; Yu, L.-D.; Liu, X.-Y.; Xu, T.-G.; et al. Design and fabrication of button-style beam position monitors for the HEPS synchrotron light facility. *Nucl. Sci. Tech.* **2022**, *33*, 141. [[CrossRef](#)]
5. Huang, X.; Jiao, Y.; Wei, Y. Preliminary investigation of the noises and updates on physics studies of FOFB in HEPS. In Proceedings of the IPAC2021, Campinas, Brazil, 24–28 May 2021; pp. 2197–2199. [[CrossRef](#)]
6. Maesaka, H. Comparison of beam diagnostics for 3rd and 4th generation ring-based light sources. In Proceedings of the IPAC2015, Richmond, VA, USA, 3–8 May 2015; pp. 3657–3661. [[CrossRef](#)]
7. Schmickler, H. Beam position measurement system design. In Proceedings of the IBIC2015, Melbourne, Australia, 13–17 September 2015; THALA01. pp. 618–624. [[CrossRef](#)]
8. Wendt, M. Overview of recent trends and developments for bpm systems. In Proceedings of the DIPAC2011, Hamburg, Germany, 16–18 May 2011; pp. 18–22.
9. Li, C.H.; Wang, H.; Zhou, N.; Li, M.; Wang, Z.; Wu, L.; Jiao, Y. Design and progress of mechanical support in HEPS. In Proceedings of the IPAC2019, Melbourne, Australia, 19–24 May 2019; pp. 4180–4182. [[CrossRef](#)]
10. Wang, B.; Duan, Z.; Ji, D.; Jiao, Y.; Zhao, Y. Progress of the first-turn commissioning simulations for HEPS. In Proceedings of the IPAC2021, Campinas, Brazil, 24–28 May 2021; pp. 1349–1351. [[CrossRef](#)]
11. Ji, D.H.; Duan, Z.; Jiao, Y.; Cui, X.; Wei, Y.; Zhao, Y. Beam performance simulation with error effects and correction on HEPS design. In Proceedings of the IPAC2018, Vancouver, BC, Canada, 29 April–4 May 2018; pp. 1349–1351.
12. He, J.; Sui, Y.-F.; Lu, Y.-H.; Yin, D.; Duan, Z.; Tian, S.-K.; Zhu, D.-C.; Zhao, Y.; Yue, J.-H.; Cao, J.-S. Preliminary study on detection and cleaning of parasitic bunches. *Nucl. Sci. Tech.* **2021**, *32*, 148–158. [[CrossRef](#)]
13. Zhang, C.; Ma, L. *Design and Development of BEPCII*; Shanghai Scientific & Technical Publishers: Shanghai, China, 2015; Chapter 2; p. 132. (In Chinese)
14. Smith, S.R. *Beam Position Monitor Engineering*; American Institute of Physics: College Park, MD, USA, 1997. [[CrossRef](#)]
15. Forck, P.; Kowina, P.; Liakin, D. *Beam Position Monitors*; CERN Accelerator School, Beam Diagnostics: Dourdan, France, 2018; pp. 187–228.
16. Marcellini, F.; Serio, M.; Zobov, M. DAFNE broad-band button electrodes. *Nucl. Instrum. Methods Phys. Res.* **1998**, *402*, 27–35. [[CrossRef](#)]
17. Shafiee, M.; Fegghi, S.; Rahighi, J. Numerical analysis of the beam position monitor pickup for the Iranian light source facility. *Nucl. Instrum. Methods Phys. Res. A* **2017**, *847*, 162–170. [[CrossRef](#)]
18. Madur, A.; Brunelle, P.; Nadji, A.; Nadolski, L. Beam based alignment for the storage ring multipoles of synchrotron SOLEIL. In Proceedings of the EPAC2006, Edinburgh, Scotland, 26–30 June 2006; WEPCH010. pp. 1939–1941.
19. Huang, X. *Beam-Based Correction and Optimization for Accelerators*; CRC Press Taylor & Francis Group: Boca Raton, FL, USA, 2020; ISBN-10: 1138353167. [[CrossRef](#)]
20. Wu, L.; Zhou, N.; Li, C.; Wang, Z. Design and test of the beam-based alignment sextupole experimental mover prototype for HEPS. *Radiat. Detect. Technol. Methods* **2021**, *5*, 570–575. [[CrossRef](#)]
21. Noelle, D.; Priebe, G.; Wendt, M.; Werner, M. BPMs with Precise Alignment for TTF2. In Proceedings of the 11th Beam Instrumentation Workshop, Knoxville, TN, USA, 3–6 May 2004. [[CrossRef](#)]
22. Wu, L.; Chen, S.; Li, C.; Qu, H.; Wang, H.; Wang, X. Research development of high precision installation and alignment system for HEPS. In Proceedings of the IPAC2015, Richmond, VA, USA, 3–8 May 2015; pp. 2924–2926. [[CrossRef](#)]

23. Lambertson, G.R. Dynamic devices-pickups and kickers. *AIP Conf. Proc.* **1987**, *153*, 1413.
24. Chung, Y.W.; Decker, G. Offset calibration of the beam position monitor using external means. *AIP Conf. Proc.* **1992**, *252*, 217–224. [[CrossRef](#)]
25. Nosych, A.; Cioeta, F.; Colldelram, C.; Crisol, A.; Falone, A.; Ghigo, A.; Iriso, U.; Mostacci, A.; Olmos, A.; Serio, M.; et al. Measurements and calibration of the stripline BPM for the ELI-NP facility with the stretched wire method. In Proceedings of the IBIC2015, Melbourne, Australia, 13–17 September 2015; pp. 423–427. [[CrossRef](#)]
26. Shinoe, K.; Nakamura, N.; Katsura, T.; Kamiya, Y. Design and Calibration of Pickup-Electrodes for Beam Position Monitoring at SOR-RING. In Proceedings of the PAC1993, Washington, DC, USA, 17–20 May 1993; pp. 2337–2339.
27. Satoh, K.; Tejima, M. Calibration of KEKB beam position monitors. In Proceedings of the PAC1997, Vancouver, BC, Canada, 12–16 May 1997; pp. 2087–2089. [[CrossRef](#)]
28. Hiramatsu, S. Beam position monitors for circular accelerators. In Proceedings of the IBIC2012, Tsukuba, Japan, 1–4 October 2012; pp. 590–601.
29. He, J.; Sui, Y.; Li, Y.; Wang, A.; Tang, X.; Zhao, Y.; Ye, Q.; Ma, H.; Xu, T.; Yue, J.; et al. Design and optimization of a Goubau line for calibration of BPMs for particle accelerators. *Nucl. Instrum. Methods Phys. Res. A* **2023**, *1045*, 167635. [[CrossRef](#)]
30. Duarte, H.; Sanfelici, L.; Marques, S. Design and impedance optimization of the SIRIUS BPM button. In Proceedings of the IBIC2013, Oxford, UK, 16–19 September 2013; pp. 365–368.
31. Olmos, A.; Alvarez, M.; Perez, F. Beam position monitors characterization for ALBA. In Proceedings of the BIW2010, Santa Fe, NM, USA, 2–6 May 2010; pp. 356–358.

Disclaimer/Publisher’s Note: The statements, opinions and data contained in all publications are solely those of the individual author(s) and contributor(s) and not of MDPI and/or the editor(s). MDPI and/or the editor(s) disclaim responsibility for any injury to people or property resulting from any ideas, methods, instructions or products referred to in the content.